Nonlinear dynamics of coupled light and particle beam propagation

Prabhat Kumar,[1] Derek Kuldinow,[2] Andres Castillo,[1] Alexandros Gerakis,[3,4] and Kentaro Hara[1,*]
[1]*Department of Aeronautics and Astronautics, Stanford University, Stanford, California 94305, USA*
[2]*Department of Physics, Yale University, New Haven, Connecticut 06510, USA*
[3]*Department of Aerospace Engineering, Texas A&M University, College Station, Texas 77843, USA*
[4]*Luxembourg Institute of Science & Technology, 4422 Belvaux, Luxembourg*

(Received 9 February 2021; accepted 18 March 2021; published 2 April 2021)

Propagation of a light beam through a collisional and inhomogeneous beam of neutral particles is investigated. The light beam can be manipulated through the refractive index that is affected by the gaseous medium. Simultaneously, neutral particles experience optical dipole force and scattering force due to atomic polarizability, leading to particle trapping. The simulation results of fully coupled light-particle propagation show agreement with experimental data from the literature. The effects of particle density, detuning frequency with respect to the resonance frequency, and light intensity on the mutual guiding of light and particle beams is studied for particle beam densities below the critical density that results in single-mode operation of optical waveguides.

DOI: 10.1103/PhysRevA.103.043502

I. INTRODUCTION

Manipulation of particles using light beams has been applied to many fields ranging from microbiology to atomic physics and polymeric studies [1,2]. For instance, optical tweezers can be used to isolate a small number of particles or molecules and manipulate them precisely [1,3]. Furthermore, light beams can be guided with waveguides with high-refractive-index contrast ratio [4–6], enabling speed-of-light communications through fiber optic cables [7]. While a collimated light beam naturally diffracts without any guiding media and particles diffuse due to their thermal motion in vacuum, precisely tailoring the coupling of the two can lead to mutually self-guided beams [8,9], allowing for unprecedented control over light-particle interaction.

The gradient of light intensity exerts an optical dipole force on a gas particle with a finite polarizability, which leads to trapping or defocusing of particles [10]. The amplification of particle density due to the optical forces was first demonstrated by Ashkin and co-workers: In their experiments, a collimated beam of sodium atoms was propagated collinearly with a converging light beam [11–14]. Trapping and defocusing of the atomic beam were observed when tuning the light frequency near resonance due to the changes in the atomic polarizability. It should be noted that such experiments were performed in relatively low-particle-density conditions, where the observed modulation of the refractive index was insignificant. Depending on the light intensity, particle density, and polarizability, the contrast in refractive index with respect to the surrounding medium (vacuum) can be large enough to guide the light beam [15,16] while simultaneously trapping the particles via optical forces.

In this paper, a self-consistent simulation that couples the light and neutral particle beams is developed and validated against experimental results from relevant studies [11–14]. The light beam propagation is modeled by solving the paraxial Helmholtz equation, which accounts for variations of refractive index due to the presence of neutral gas particles. The transparent boundary condition [17,18] is revised and implemented, enabling stable numerical calculations. For the particle dynamics, optical forces on two-level atoms are summarized and implemented. Both dipole and scattering forces are taken into consideration. In addition, intermolecular collisions are taken into account in the particle beam using the direct simulation Monte Carlo method. It should however be noted that the present study focuses on a high-Knudsen-number case; thus the intermolecular collisions are considered negligible under the conditions presented in this paper.

Fully coupled simulations of light-particle interaction are performed in a configuration similar to the experimental setup proposed by Pearson *et al.* [14], where a converging light beam copropagates with a beam of neutral sodium atoms. In Sec. II the physical processes involved in particle-light interaction are reviewed. Section III discusses the computational model and implementation. In Sec. IV simulation results show good agreement with experimental observations. Furthermore, the degree of collimation of both the particle and light beams with respect to propagation in the vacuum condition is investigated by varying the light intensity, light frequency, and particle density.

II. THE PHYSICS OF LIGHT-PARTICLE COUPLING

A. Light propagation

To model the propagation of a light beam, we employ an axisymmetric paraxial Helmholtz equation [19]. The paraxial equation is derived from the Maxwell equations assuming that

*kenhara@stanford.edu

2469-9926/2021/103(4)/043502(10)

the light intensity evolves slowly compared to the dynamics of particles and that the beam envelope changes slowly with respect to the wavelength. The first assumption is valid in the case that the refractive index changes slowly with respect to the speed of light, which is the case for a slowly evolving medium. The second assumption, namely, the slowly varying envelope approximation, is valid for a forward-propagating wave predominantly in one direction. The light beam is described by the complex amplitude of the electric field E. The paraxial Helmholtz equation can be written as

$$\nabla_\perp^2 E + 2ik_0\frac{\partial E}{\partial z} + k_0^2(n^2-1)E = 0, \quad (1)$$

where $\nabla_\perp^2$ is the Laplacian in the transverse direction, z is the direction of beam propagation, $k_0 = 2\pi/\lambda$ is the wave number in vacuum, λ is the wavelength, and n is the complex refractive index. The refractive index is dependent on the medium's density, polarizability, and light intensity, which will be discussed in the next section. Note that an analytical solution of Eq. (1) can be obtained in the vacuum condition, i.e., $n = 1$. Additionally, the light intensity can be given by $I = \frac{1}{2}\epsilon c|E|^2$, where ϵ is the permittivity of the medium and c is the speed of light. The net power can be calculated by integrating I over an area.

B. Refractive index

Propagation of electromagnetic waves through a medium can be described by the electric field $\mathbf{E}(\mathbf{r}, t)$ and induced polarization $\mathbf{P}(\mathbf{r}, t)$, where $\mathbf{r}$ is the position and t is time. The frequency-dependent field and polarization are related by $\mathbf{P}(\omega) = \epsilon_0\chi(\omega)\mathbf{E}(\omega)$, where ϵ_0 is the vacuum permittivity, ω is the light frequency, and χ is the electric susceptibility, which measures the ability of a medium to become transiently polarized [20–22]. For a rarefied medium such as low-density gases, susceptibility can be written in terms of polarizability as $\chi(\omega) = \frac{N}{\epsilon_0}\alpha(\omega)$, where N is the particle density and $\alpha(\omega)$ is the mean complex atomic polarizability. In view of the relationship $\chi = n^2 - 1$, the refractive index n is then given by

$$n^2 = 1 + \frac{N\alpha}{\epsilon_0} \quad (2)$$

as a function of ω and is a complex number $n = n' + in''$. The real part of the refractive index n' is associated with changes in the phase speed of the wave and leads to refocusing or guiding of the light. The imaginary part n'' represents the attenuation by absorption and scattering. Equation (2) provides a relationship between particle density, polarizability, and the refractive index, which can be used to model the nonlinearly coupled light-particle interaction.

C. Atomic polarizability

The complex atomic polarizability of a two-level atom for frequencies near the atomic resonance is expressed as [11,12,22,23]

$$\alpha = \alpha' + i\alpha'' = \frac{4\pi\epsilon_0}{1+p(f)}\frac{\lambda_0^3}{16\pi^3}\frac{\gamma_N}{2}\frac{-(f-f_0)+i\left(\frac{\gamma_N}{2}\right)}{(f-f_0)^2+\frac{\gamma_N^2}{4}}, \quad (3)$$

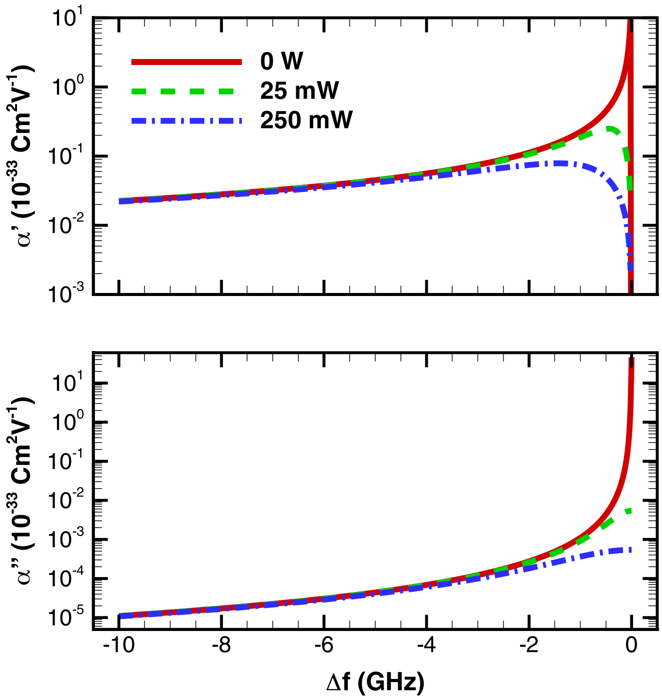

FIG. 1. Real (α') and imaginary (α'') parts of frequency-dependent polarizability of sodium atoms for several light powers near resonance. The detuning below resonance, i.e., $\Delta f < 0$, corresponds to a positive α', while detuning above resonance yields negative α' (not shown in this figure).

where the external laser frequency $f = \omega/2\pi$ is assumed to be near the resonance frequency $f_0 = \omega_0/2\pi$, λ_0 is the resonance wavelength, γ_N is the natural linewidth, and

$$p(f) = \frac{I}{I_{\text{sat}}}\frac{\gamma_N^2/4}{(f-f_0)^2+\gamma_N^2/4} \quad (4)$$

is the saturation parameter. Here I_{sat} is the saturation intensity given by

$$I_{\text{sat}} = \frac{2\pi^2 hf\gamma_N}{\lambda^2}, \quad (5)$$

where h is the Planck constant. It should be noted that the polarizability values obtained using Eq. (3) are consistently three time smaller than the values reported in the literature [24] at light frequencies off-resonance, e.g., $f \in$ [192.9 THz, 999.3 THz]. There is a prefactor of 3 in the static (i.e., off-resonance) polarizability estimate which arises from orientation of atoms with light for the maximum absorption cross section [25].

The real and complex parts of polarizability calculated from Eq. (3) are shown in Fig. 1 for sodium atoms within a range of detuning frequencies $\Delta f = f - f_0$ below resonance (i.e., $\Delta f < 0$). The resonance frequency of the $3\,^2S_{1/2} \rightarrow 3\,^2P_{3/2}$ transition is 508.9 THz, corresponding to a 589-nm wavelength. Here $\gamma_N = 9.795$ MHz and I is calculated assuming a Gaussian beam: $I = 2P/\pi w_0^2$, where w_0 is the beam waist. For this case, the beam waist w_0 is 100 μm (taken from Pearson's experiments [14]). Note that the static polarizability of sodium is 2.68×10^{-39} C m^2 V^{-1} [26], which is approximately six orders of magnitude smaller than the dynamic polarizability near the atomic resonance. In this paper, we primarily focus on the validation of the computational model against the experimental results near but below resonance (-10 GHz $< \Delta f < 0$ GHz), resulting in $\alpha' > 0$.

D. Optical forces on neutral gas particles

The two types of optical forces exerted by light on neutral particles include (a) the optical dipole force, which arises from the Lorentz force acting on a moving charge dipole, and (b) the scattering force due to absorption and spontaneous emission of photons by particles. The optical dipole force is given by

$$\mathbf{F}_{\text{dip}} = -\nabla U_{\text{dip}}, \tag{6}$$

where U_{dip} is the potential of the dipole moment $\mathbf{p} = \alpha' \mathbf{E}$ induced by the driving field $\mathbf{E}$:

$$U_{\text{dip}} = -\tfrac{1}{2}\langle \mathbf{p} \cdot \mathbf{E} \rangle. \tag{7}$$

Here, the angular brackets denote the time averaging over the high-frequency terms [21]. The dipole force can be expressed in terms of the real part of polarizability as

$$\mathbf{F}_{\text{dip}} = \frac{1}{2\epsilon_0 c}\alpha' \nabla I. \tag{8}$$

The dipole force is proportional to and acts in the direction of the laser intensity gradient and pushes atoms in the regions of higher intensity for laser frequencies tuned below resonance.

The other important force for light-particle interaction is the scattering force due to particles absorbing and reemitting photons, e.g., spontaneous emission, consequently undergoing two processes of momentum transfer with a photon. The mean scattering force $\mathbf{F}_{\text{scat}}$ exerted by the laser, averaged over its optical period, can be written as [12,25]

$$\mathbf{F}_{\text{scat}} = \hbar \mathbf{k} \frac{\Gamma}{2} \frac{p(f)}{1 + p(f)}, \tag{9}$$

where $\hbar = h/2\pi$ is the reduced Planck constant, $\mathbf{k}$ is the wave vector, and $\Gamma = 2\pi\gamma_N$ is the spontaneous decay rate of the excited state. In fact, the scattering force has two contributions [12,13]. One arises from conservation of momentum between the photons and particles during the absorption of light by an atom, which effectively pushes the particles in the direction of the light propagation. The other contribution is the scattering due to the spontaneous emission, assuming that photons are emitted isotropically, i.e., in a random direction [27,28]. This results in *heating* of the atoms limiting the degree to which an atomic beam can be focused [28]. For high light intensities, $p(f)$ in Eq. (4) is large and the maximum scattering force the laser can exert on the atom is $\hbar \mathbf{k} \frac{\Gamma}{2}$. From Eqs. (3)–(5) and (9), the scattering force exerted on a particle by the light can be expressed in terms of the imaginary part of polarizability as

$$\mathbf{F}_{\text{scat}} = \frac{k_0}{\epsilon_0 c}\alpha'' I \hat{\boldsymbol{k}}, \tag{10}$$

where $\hat{\boldsymbol{k}}$ is the direction in which the scattering force is applied.

III. COMPUTATIONAL MODEL

A. Field solver

The paraxial Helmholtz Eq. (1) is solved to obtain the spatial distribution of an arbitrary initial electric field profile propagated through a spatially heterogeneous dielectric medium. Second-order accurate discretization of $\nabla_\perp$ is implemented. It is observed from the present simulations that spurious numerical oscillations occur using the second-order-accurate Crank-Nicolson method particularly in the presence of the gaseous medium. The first-order backward Euler method [29] is therefore used for this paper since it is found to be robust for a wide range of parameters.

B. Revisiting the transparent boundary condition

The Crank-Nicolson scheme, together with the transparent boundary condition (TBC) [17,18] for outgoing radiation, is widely used for finite-difference beam propagation and is revisited here. Consider a diverging laser beam propagating in the z direction with complex axial and radial wave numbers k_z and k_r, respectively, near the boundary node. The TBC enforces that the beam behaves as a plane wave, i.e., a complex exponential near the boundary,

$$\xi_M^j = \frac{E_M^j}{E_{M-1}^j} = \exp\left(ik_r^j \Delta r\right), \tag{11}$$

where the superscript j denotes the nodes in the axial direction, the subscripts $m = M, M-1$ correspond to the radial nodes on the boundary and one node interior, respectively, and Δr is the cell size in the radial direction. Although the procedure above is fully adapted to well-collimated beams, its effectiveness is somewhat limited for simulation of wide-angle propagation waves and several improvements have been proposed [30,31]. Considering that one knows the full profile of E_m^j $(m = 1, 2, \ldots, M)$, the boundary condition needed is for the next axial location, i.e., E_M^{j+1}.

Before application of Eq. (11) to the next axial location $j+1$, k_r can be found using the solution at the jth axial node and geometrical considerations, which take into account the relative grid sizes and the angle at which the beam wave front approaches the boundary. The real and imaginary parts of these wave-vector components must satisfy the dispersion relation $k_r^2 + k_z^2 = k^2$, where $k = k_0\eta$, in an inhomogeneous medium. Here we define $k_r = k_r' + ik_r''$ and $k_z = k_z' + ik_z''$, where the primed and double primed quantities are the real and imaginary parts, respectively. Using Eq. (11), the real and imaginary parts of k_r^j can be obtained. Then k_z' and k_z'' can be readily obtained by solving the system of equations

$$(k_r')^2 - (k_r'')^2 + (k_z')^2 - (k_z'')^2 = \text{Re}(k^2), \tag{12}$$

$$k_r' k_r'' + k_z' k_z'' = \tfrac{1}{2}\text{Im}(k^2), \tag{13}$$

where $\text{Re}(k^2)$ and $\text{Im}(k^2)$ denote the real and imaginary parts of k^2, respectively. The real part of the wave vector signifies the propagation of the wave front in the direction of $\mathbf{k}'$, while the imaginary part $\mathbf{k}''$ only affects the attenuation of the beam. If $k_r' > 0$, the wave front reaching the boundary at the next axial location $j+1$ can be considered to originate from a distance ΔR away from the boundary at the axial location j,

$$\Delta R = \frac{(k_r')^j}{(k_z')^j}\Delta z = a\Delta r, \tag{14}$$

where a is a real number and Δz is the cell size in the longitudinal direction, assuming a uniform mesh. If $k_r' < 0$, the wave comes from outside the computational domain, which needs to be *a priori* known. The boundary condition for E_M^{j+1}, i.e., ξ_M^{j+1}, is obtained by interpolating or extrapolating the wave front from the jth step solution

$$\xi_M^{j+1} = \frac{E_M^{j+1}}{E_{M-1}^{j+1}} = \begin{cases} \xi_{M-[a]}^j & \text{if } a \geqslant 1 \\ a\xi_{M-1}^j + (1-a)\xi_M^j & \text{if } 0 < a < 1. \end{cases}$$

Here $[a]$ denotes the smallest integer less than or equal to a. Note that for a converging light beam that is coming from outside the domain boundary, i.e., $\Delta R < 0$ from Eq. (14), the boundary condition is set as $\xi_M^{j+1} = 0$ for simplicity, i.e., $E_M^{j+1} = 0$, as can be seen from Eq. (11).

C. Particle dynamics

The computational grids are kept uniform in the axial direction z. However, a uniform discretization in the radial direction leads to large numerical noise due to particle statistics near the axis of propagation ($r = 0$). This is addressed by employing a nonuniform discretization in the radial direction based on an equal cylindrical node volume formulation [32].

Particles are injected into the domain with a given velocity distribution function. At each time step Δt, the forces on the particles are calculated, the velocities are updated by $d\mathbf{v}/dt = \mathbf{F}/m$, and the positions are updated as $d\mathbf{r}/dt = \mathbf{v}$, which is similarly done in plasma simulations [33–35]. To determine the total force $\mathbf{F} = \mathbf{F}_{\text{dip}} + \mathbf{F}_{\text{scat}}$ on the particle, the gradient of the intensity (for $\mathbf{F}_{\text{dip}}$) and the intensity itself (for $\mathbf{F}_{\text{scat}}$) are calculated at each of the points on the computational grids using the second-order finite difference and are linearly interpolated to the (r, z) position of the particle. Updated particle positions are then linearly interpolated to compute the density distribution on the computational grids.

The direct simulation Monte Carlo (DSMC) method is implemented to model collisions between the neutral particles in the beam. The DSMC has been successfully implemented in a variety of flow applications [36], and it conserves energy and momentum, unlike the Monte Carlo collision model in low-temperature plasmas [37]. Due to its relative advantage of computational cost, the no-time-counter model is used [38]. For a single species flow, this model minimized the total number of particle pairs to check for a collision using the expression

$$N_c = \frac{N_p(N_p - 1)F_N(\sigma c_r)_{\max}\Delta t}{2V_c}, \tag{15}$$

where N_p is the number of particles in a cell, F_N is the macroparticle weight, σ is the cross section, c_r is the relative velocity between two particles, V_c is the cell volume, and Δt is the time step. Equation (15) effectively represents the total number of possible collision pairs $\frac{1}{2}N_p(N_p - 1)$ multiplied with the maximum rate coefficient of a collision $(\sigma c_r)_{\max}$. By choosing N_c pairs to check whether the particles actually collide or not, the probability of a collision event that actually occurs within the DSMC becomes

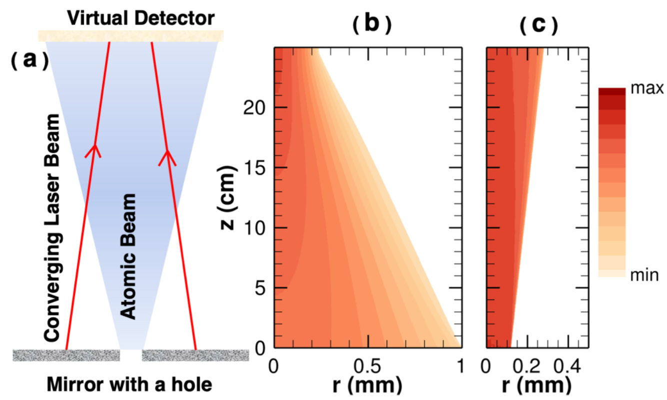

FIG. 2. Simulation setup. (a) Schematic of light-particle coupling. The mirror is used to generate a converging light beam, which copropagates with the particle beam emerging from an atomic beam source 55 cm upstream from the mirror and enters the computational domain through a 230-μm hole in the mirror. (b) Light intensity in the absence of particles. (c) Number density of an effusing particle beam without any collisions and light-particle interactions.

$$P = \frac{\sigma c_r}{(\sigma c_r)_{\max}}, \tag{16}$$

where the numerator values are obtained from the chosen particle pair. Once N_c is determined, two random particles are selected within the cell and their collision probability is calculated. Using the acceptance-rejection technique, the collision occurs if the probability is larger than a random number between 0 and 1. Once a collision occurs, the postcollisional velocities are calculated and update the particle velocities. This process is repeated until N_c pairs have been checked. Afterward, the maximum value for σc_r from all the checked pairs is updated as $(\sigma c_r)_{\max}$ for the following time steps.

D. Simulation setup

We follow the experiments of Pearson *et al.* as described in Ref. [14]. In their experiment, a linearly polarized laser was reflected off of a 3-mm-thick slanted mirror having a 230-μm hole. The laser was superimposed upon an effusive beam of sodium atoms having a temperature of 773 K, emerging from an atomic source 55 cm upstream of the mirror (not shown in Fig. 2), which enters the field of the laser through the hole in the mirror.

The simulation setup, as shown in Fig. 2, includes a Gaussian laser source of wavelength 589 nm, which is focused to a waist of $w_0 = 100$ μm onto a virtual detector that is set after 25 cm of the interaction region. In the simulation, an effusive beam of neutral sodium atoms is injected through the mirror hole. Distribution of the particle beam to be injected is determined by the temperature, mirror hole dimensions, and the distance of the mirror from the atomic source as listed in the preceding paragraph. Changes in the velocities of these atoms due to interaction with the mirror-hole walls are accounted for assuming diffusive reflection.

The C standard general utilities library is used to generate random numbers for particle injection, intermolecular collisions, and the isotropic scattering force due to the emitted photons. The computational domain has a longitudinal size of $z_{\max} = 25$ cm, which is uniformly discretized using $J = 250$ cells. The radial domain is discretized as $\Delta r_m = r_{\max}(\sqrt{m} - \sqrt{m-1})/\sqrt{M}$, where $r_{\max} = 1.0$ mm is the radial domain size, j is the number of cells ($m = 1, 2, \ldots, M$), and $M = 2000$ is the number of cells in the radial direction. This technique minimizes the numerical noise along the axis [32]. The time step is $\Delta t = 1$ μs and the computational results are found to reach steady state at $t = 20$ ms. The results are averaged over 5000 time steps once the simulation reaches steady state.

A beam of neutral sodium atoms is focused using light tuned below but near the $3\,^2S_{1/2} \rightarrow 3\,^2P_{3/2}$ resonance frequency of 589 nm. The detuning frequency and light power are varied. The results using $P = 25$ and 250 mW are shown in this paper.

The particle density is set below the critical density (cf. waveguide theory [39]), which provides a single-mode operation in the optical fiber. This is often characterized by the V-number given by $V = \frac{2\pi a_0}{\lambda}\sqrt{n_1^2 - n_0^2}$, where a_0 is the radius of the fiber and n_1 and n_0 are the refractive indices of the fiber and the housing (vacuum in our application), respectively. It is observed from waveguide theory that $V = V_1 = 2.4$, corresponding to the first zero of the Bessel function, is a limit to the single-mode operation. If the refractive index is made larger or the aperture of the optical fiber is made smaller, the V-number increases and the light propagation follows a multimode operation. Therefore, the critical density for single-mode operation is given by

$$N_c = \frac{V_1^2 \lambda^2 \epsilon_0}{4\pi\alpha'\left(\pi w_0^2\right)}, \tag{17}$$

which is inversely proportional to the real part of polarizability.

The coupled simulation is validated for particle beams that are below the critical density, which is consistent with the previous experimental conditions [11–14]. For the conditions listed above, the critical density is $N_c \approx 10^{17}$ m^{-3}. Here we present two cases, (i) $N_0 = 1.0 \times 10^{14}$ m$^{-3} \ll N_c$ (low-density regime, estimated from Pearson's experiment [14]) and (ii) $N_0 = 5.0 \times 10^{16}$ m$^{-3} \approx N_c$ (higher-density regime), where N_0 is the beam density at the injection, i.e., at the mirror hole. The simulation results and physical processes for particle density much higher than the critical density is reserved for future work.

IV. RESULTS

A. Low-density regime

Figure 3 shows the steady-state laser intensities [Figs. 3(a i) and 3(a ii)] with corresponding particle densities [Figs. 3(b i) and 3(b ii)] for the 25-mW and 250-mW cases, respectively. The light amplification, shown in Fig. 3(a iii), is defined as

$$\zeta_I = \frac{I(N, r, z)}{I(N_0 = 0\ \mathrm{m}^{-3}, r = 0\ \mathrm{mm}, z = 25\ \mathrm{cm})}, \tag{18}$$

i.e., the ratio of light intensity in the gaseous medium to that in a vacuum condition at $r = 0$ cm and $z = 25$ cm. It can be seen that the converging light amplification is virtually unchanged in the presence of a particle density of $N = 10^{14}$ m^{-3} regardless of the light power. The refractive index remains close to unity ($\eta \approx 1$) at a nominal density of 10^{14} m^{-3}, which is three orders of magnitude lower than the critical density.

The density amplification, shown in Fig. 3(b iii), is given similarly to the light amplification as

$$\zeta_N = \frac{N(I, r, z)}{N_0(I = 0\ \mathrm{W/m^2}, r = 0\ \mathrm{mm}, z = 25\ \mathrm{cm})}, \tag{19}$$

i.e., the particle beam density normalized with the density at $r = 0$ cm and $z = 25$ cm in the absence of the light, corresponding to the pure effusion case. This metric is chosen to illustrate how much trapping of particles resulted from the light-particle interaction. Similar to the light amplification, the density amplification without the use of light (i.e., 0 W) is unity at $r = 0$ cm and $z = 25$ cm. When a light beam is applied, the optical dipole force of the light pushes the atoms in the region of higher intensity. At the same time, scattering force acts on the particles in a random direction via spontaneous emission after the light is absorbed by the particle. This results in some particle leaving the trap created by the dipole force and appear as fringes, as can be seen in Fig. 3(b i).

With an increase in light power from 25 mW to 250 mW, stronger focusing of the beam is achieved. As shown in Fig. 3(b iii), the particle beam amplification for 25-mW and 250-mW light beams is observed to be ∼10.5 and ∼28 at maximum, respectively. The detuning frequency is further varied for the 25-mW and 250-mW light cases, and the result is shown in Fig. 4. Under the present conditions and setup, the simulation results show that the *optimal* detuning frequencies of 2.5 GHz for the 25-mW light and 7 GHz for the 250-mW light maximize the amplification of the particle density, respectively. These results are in good agreement with experimental observations, where density amplifications of 12 and 32 are observed for the 25-mW and 250-mW cases, respectively [14]. Note that the exact quantitative comparisons between the simulation and experiments are difficult to make since the numerical setup is likely different from the exact experimental conditions, e.g., particle beam profile and velocity distribution functions. In fact, later in this paper, we show that the particle density has a significant effect on the dynamics of both the light and particle beams. It should still be noted that good qualitative agreement is obtained if one considers the ratio of the amplification between 25 and 250 mW, which is equal to 2.67 for both the experimental and simulation cases.

Figure 4 shows the overall density amplification over a wide range of detuning frequencies. The amplification approaches a small value near resonance since the scattering force is large due to the large absorption, i.e., large α'', as shown in Fig. 1. The smallest detuning frequency shown in Figs. 4(a) and 4(b) correspond to 0.1 and 1.0 GHz, respectively. In the other limit, at off-resonance, the amplification converges to unity, i.e., no trapping or defocusing, since the optical trapping (due to α') and scattering forces (due to α'') both become orders of magnitude smaller than near-resonance values. The close-ups in the insets in Fig. 4 show the mean value and the standard deviations of the results for each detuning frequency near the maximum density amplification. In the simulations, it is observed that the density amplification

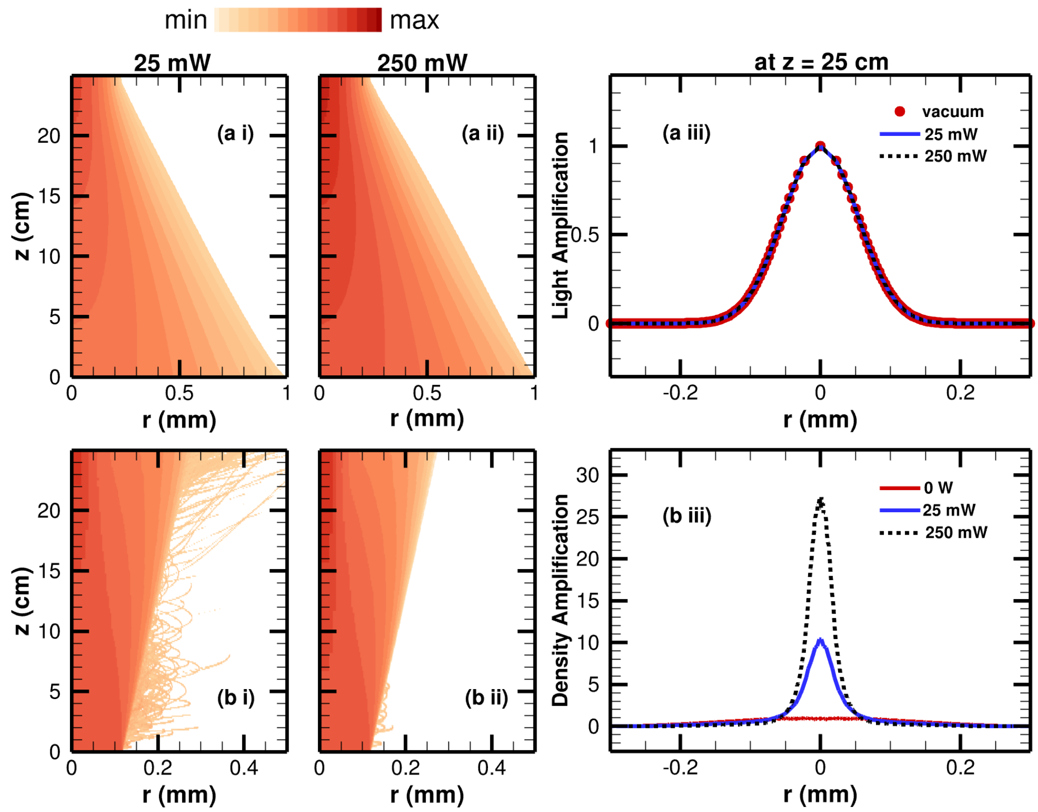

FIG. 3. Trapping of a particle beam by the optical forces of a laser for $N_0 = 1.0 \times 10^{14}$ m^{-3}. Light is tuned to a frequencies of 2 and 7 GHz below the sodium D_2 resonance for light power of (a) 25 mW and (b) 250 mW, respectively. (a i) and (a ii) Light intensity. The minimum and maximum values correspond to 10 and 1.0×10^8 W m^{-2}, respectively. (b i) and (b ii) Particle beam density. The minimum and maximum values correspond to 1.0×10^{10} and 1.0×10^{15} m^{-3}, respectively. The colormap is in logarithmic scale. (a iii) Light amplification at the exit plane, i.e., light intensity normalized by the maximum light intensity at $z = 25$ cm of the vacuum condition. (b iii) Density amplification at the exit plane, i.e., particle density normalized by the maximum density at $z = 25$ cm in the absence of light. Amplifications of 10.5 and 28 are observed for the 25-mW and 250-mW cases, respectively.

slightly varies with each simulation run due to the randomness associated with the scattering and collisional events. Thus, the simulation is repeated approximately ten times under the same conditions with different seed numbers of the random number generator to obtain sufficient statistics for each detuning frequency. The results illustrate that there is an optimal frequency at which the peak amplification occurs. For the 25-mW case, the density amplification reaches 10.5 around $\Delta f = -2.5$ GHz. For the 250-mW case, the average density amplification is largest around 27 between $\Delta f = -6$ and -10 GHz. It can be concluded that the optimal detuning frequency for maximum density amplification is determined due to the balance between the optical dipole force (dependent on α') and scattering force (dependent on α''). It should be noted that a theoretical expression for the optimal detuning frequency Δf_{opt} to maximize the beam density amplification is derived as a function of incident particle beam density distribution [13]:

$$\Delta f_{\text{opt}} = \left(\frac{h\gamma_N^2}{6\pi m^2 c}\right)^{1/2}\left(\frac{P}{v_0^3 \Delta\theta^2}\right)^{1/2}, \tag{20}$$

where $v_0 \Delta\theta$ is the maximum initial transverse speed of the atom with $\Delta\theta$ the half angular divergence of the atomic beam. However, as mentioned above, exact quantitative agreement with experimental values is difficult to achieve since the theory simplifies some key physical processes, including the particle beam spread in the transverse direction to be a single value, which is likely not the case in a realistic condition. Nevertheless, the optimal detuning frequencies of 2.5 and 7 GHz from the present simulation results are close to the values obtained from the simplified theoretical formula (2.26 and 7.15 GHz, respectively), when $\Delta\theta = 3.0 \times 10^{-4}$ rad. This value of $\Delta\theta$ was obtained from the half angle of the atomic beam divergence in our simulation.

In addition, Fig. 5 shows the effect of the Doppler redshift due to the nonstationary atomic beams on the particle trapping under the same simulation conditions as in the 25-mW case in Fig. 3. The angular frequency seen in the frame of reference of an atom moving with velocity $\mathbf{v}$ is

$$\omega' = \omega - \mathbf{k} \cdot \mathbf{v}, \tag{21}$$

where $\mathbf{k}$ is the wave vector of the laser. The effective frequency is smaller when the light and particle beams co-propagate ($\mathbf{k} \parallel \mathbf{v}$). This shift in the effective frequency is unique to each atom as they interact with the radiation at their own velocities. Thus, the polarizability on each particle accounts for the Doppler effect in Eq. (3). However, as shown in Fig. 3(a iii), the light intensity remains nearly identical; thus the refractive index is assumed to be unaffected when $N \ll n_c$.

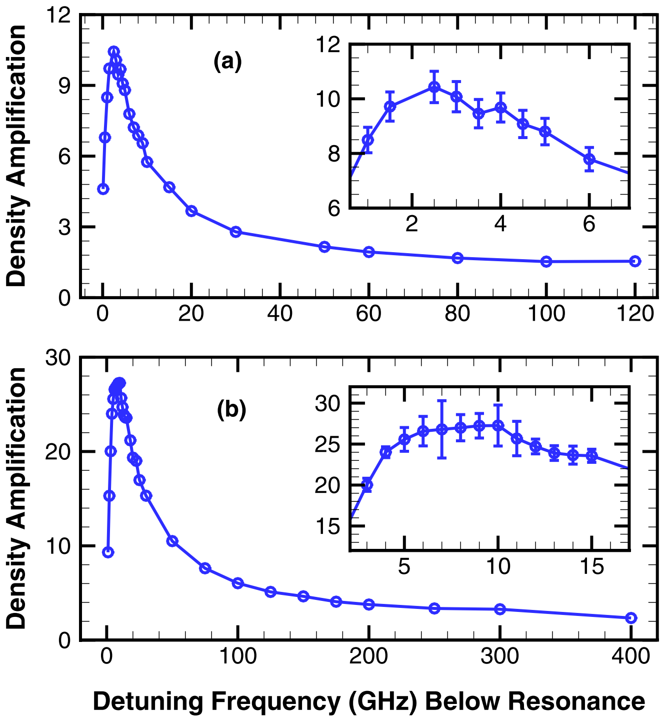

FIG. 4. Effect of light detuning frequency on the density amplification for (a) 25-mW and (b) 250-mW lasers. The insets show the close-up near the maximum amplification. The simulation is repeated approximately ten times for each detuning frequency and the statistical mean and standard deviation are shown.

It can therefore be considered that the Doppler effect on the light propagation is negligible in the low-particle-density case. The broadening and shift of the spectral line due to the Doppler effect modifies the real and imaginary parts of the polarizability, leading to changes in both the optical dipole force and scattering force. It is observed from Fig. 5 that the atoms undergo a slightly stronger focusing *without* the Doppler effect, primarily due to the larger α'. Its effect on focusing is observed to be approximately 10% in the present configurations.

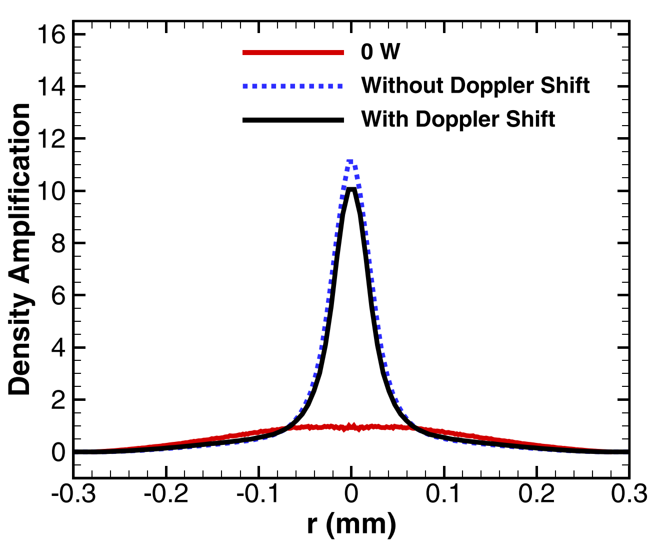

FIG. 5. Effects of Doppler shift on particle trapping for the 25-mW case: blue dotted line, without the effect of the Doppler shift, and black solid line, including the Doppler shift effects, which is identical to the result shown in Fig. 3(b iii) for the 25-mW case. As a reference, the no-light condition (0 W) is shown as a red solid line.

B. Higher gas density

In order to investigate the effects of the particle density, thus increasing the refractive index, the interaction of the light and sodium atomic beams is investigated for particle number density $N = 5.0 \times 10^{16}$ m^{-3}, which is two orders of magnitude higher than what is used in the preceding section. While the density is still below the critical density $N_{\rm crit} = 1.37 \times 10^{17}$ m^{-3} so that multimode coupling [20] is not observed, the larger refractive index results in the amplification of the light beam and not only the particle beam. It should be noted that $n - 1 \approx N\alpha/2\epsilon_0 \sim 5.0 \times 10^{-7} \ll 1$ [cf. Eq. (2)]. All other physical and numerical parameters are kept the same as in the preceding section to quantify the effect of the increase in the atomic beam density.

Figure 6 shows the time-averaged steady-state density profile and corresponding light intensity distribution for two different laser powers, 25 and 250 mW, respectively. At this density, the nonlinear coupling between the laser and particle beam is more evident. In comparison to the lower-particle-density cases, the particles are similarly trapped due to the light beam, but most notably the light beam is distorted due to the particle beam, as shown in Figs. 6(a i) and 6(a ii).

The light amplification at the exit, $z = 25$ cm, in Fig. 6(a iii) (for $N = 5 \times 10^{16}$ m^{-3}) can be compared to Fig. 3(a iii) (for $N = 1 \times 10^{14}$ m^{-3}). The overall shape (in the core) maintains a Gaussian-type distribution in the radial direction. However, most interestingly, light amplification of 1.7 is observed at 25-mW laser power in the high-particle-density case. Light amplification of 1.2 is also observed for the 250-mW case, but this modest change is likely due to the efficient particle trapping resulting in a narrow channel of the particle beam in the core as a waveguide. Thus, it can be considered that the *profile* of the particle beam in addition to the particle density plays an important role in intensifying the light beam. Due to the high particle density in the core of the copropagating beam, there is also some evidence of additional rays of the light beam, as can be seen from the tail of the light beam in Figs. 6(a i) and 6(a ii).

The corresponding particle densities are shown in Figs. 6(b i) and 6(b ii). The density amplification at the exit, $z = 25$ cm, is shown in Fig. 6(b iii). A similar particle density profile can be seen with these higher-density cases compared to the lower-density cases; particularly in Fig. 6(b i), the particle trajectories due to the scattering from the light beam are observed. Most notably, there is a 50% increase in the maximum density amplification at the higher density compared to the lower-density case for 25-mW light. This is likely because the light is more intensified due to the large refractive index, leading to further trapping of particles. Thus, the nonlinear coupling of the light and particles is evident. However, the density amplification for 250-mW light is not significantly affected by the particle number densities. This is due to the fact that the dipole potential set by the light beam is so large that the particles are deeply trapped within the potential well.

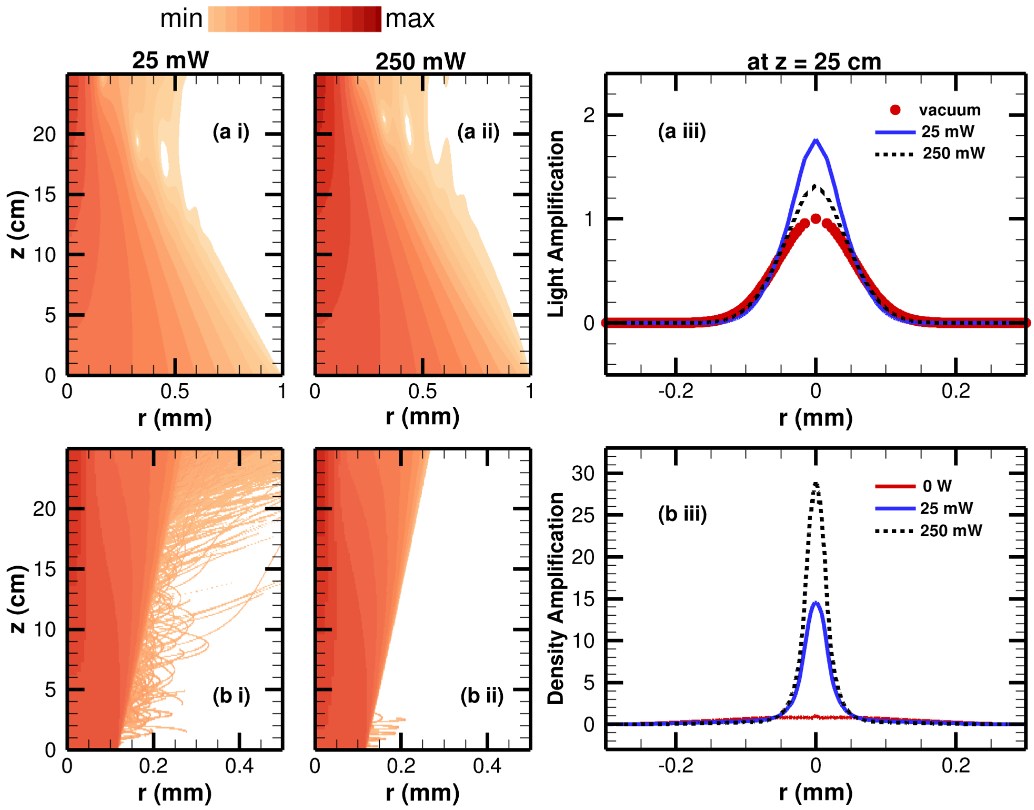

FIG. 6. Mutual guiding of sodium atom beam and laser for atomic beam density $N_0 = 5.0 \times 10^{16}$ m^{-3}. (a i) and (a ii) Light intensity. The minimum and maximum values correspond to 10 and 1.0×10^8 W m^{-2}, respectively. (b i) and (b ii) Particle beam density. The minimum and maximum values correspond to 1.0×10^{10} and 5.0×10^{17} m^{-3}, respectively. The colormap is in logarithmic scale. (a iii) Light amplification by 72% and 26% at the exit plane is observed for 25-mW and 250-mW lights, respectively. (b iii) Density amplification by factors of 14.9 and 29.8 at the exit plane is observed for 25-mW and 250-mW lights, respectively.

To explain the dependence of light power on the light amplification due to the presence of the particle beam, we consider the transverse (i.e., radial) velocity change of the particle beam via the optical dipole force exerted by the converging light beam, assuming that the injected particle beam radius is approximately equal to the light beam waist. Here it is hypothesized that the maximum *spatial* overlap between the particle beam and light leads to the coupled guiding effects. When the inward velocity change due to the dipole force coincides with the initial outward velocity spread from the effusing particle beam, the particles are neither undertrapped or overtrapped with respect to the light beam profile and therefore achieve an optimal profile as a guiding medium for the light propagation. A particle in the system will gain a velocity increase inward in the radial direction by the optical dipole force

$$\Delta v_r = \frac{F_{r,\mathrm{dip}}}{m}\Delta T = \frac{\alpha'}{2m\epsilon_0 c}\nabla_r I \Delta T, \tag{22}$$

where ΔT is the time spent by the particle in the region of light intensity before it reaches the focus position at $z = 25$ cm. An order-of-magnitude analysis can be made using Eq. (22). The characteristic transverse velocity spread of the effusing particle beam is set approximately to $\Delta v_{r,\mathrm{init}} = 1$ m/s (which is two to three orders of magnitude smaller than the axial particle velocity). Under the present configuration, $\alpha' \approx 10^{-34}$ F m^2, $m \approx 4 \times 10^{-26}$ kg, $\nabla_r I \approx I_0/w_0 \approx 10^8$ W/m^2 for 25-mW light power, and $\Delta T \approx z_R/v_z$ (here $z_R = 5.3$ cm is the Rayleigh range and $v_z \approx 250$ m/s is the characteristic axial speed v_z). Using these values in Eq. (22), we find $\Delta v_r \approx 1.6$ m/s, which can be shown to be on the same order as $\Delta v_{r,\mathrm{init}}$. This analysis can be extended to the 250-mW laser power case, where the velocity change Δv_r will be a magnitude larger, i.e., $\Delta v_r \approx 16$ m/s due to the converging dipole force, leading to $\Delta v_r \gg \Delta v_{r,\mathrm{init}}$. Thus, the majority of the particles remain deeply trapped close to the axis of propagation, which is consistent with the observations in Fig. 6(b ii).

This validated computational model will serve as a tool to study precise tailoring of light and particle beams, which can lead to mutually self-guided beams, allowing for unprecedented control over light-particle interactions. For a diverging laser beam propagating through a gaseous medium, scattering of particle and optical beams is expected and the maximum distance of mutual guiding between the light and particle beams can be estimated. It should also be noted that an atomic medium can attain a refractive index much larger than unity with an increase in gas density [40,41], which is reserved for future work.

V. CONCLUSION

A computational model and simulation framework were developed and presented to investigate the copropagation of the light beam through an inhomogeneous beam of neutral particles. The coupled equations governing the particle motion and light wave were derived from Maxwell equations for propagation in heterogeneous media. We discretized the paraxial Helmholtz equation on a two-dimensional nonuniform axisymmetric mesh. The transparent boundary condition was revisited and implemented to minimize reflections of the light beam at the boundary of the computational domain. Particles were moved by taking into account the dipole and scattering forces.

Simulations were performed to model the experiment described by Ashkin and co-workers. The results were compared to experimentally measured amplification of the sodium atom density for particle beam densities below the critical density, which is the density at which the waveguiding mode is known to achieve single-mode operation. Contributions of dipole and scattering forces were analyzed and the effect of the Doppler frequency shift was quantified. Simulation results showed great agreement with the experimentally measured density amplification for a laser tuned below the $3\,{}^2S_{1/2} \rightarrow 3\,{}^2P_{3/2}$ resonance frequency of 589 nm. The dependence of the detuning frequency on density amplification was also investigated. The present simulations showed that the detuning frequencies of 2.5 GHz for 25-mW light and 7 GHz for 250-mW light maximize the amplification for the parameters simulated, which qualitatively agrees with the experimental observations.

With the validated computational model, the simulation results at a higher particle density approaching the critical density demonstrated the effect of coupled light-particle propagation. The particle and light amplification exhibited similar behavior regardless of the particle atom density in the 250-mW case, since the light power was large enough that particles became deeply trapped inside the dipole potential. Most interestingly, a nonlinear amplification in both the particle beam density and light intensity was observed for the 25-mW case due to the nonlinear coupling of the two beams. It was hypothesized in this paper that the nonlinear effects play an important role when the particle spatial profile matches the profile of the light propagation. A simple analysis based on the velocity spread (balance between the inward velocity change due to optical dipole force and the initial outward velocity spread due to the effusing particle beam) was provided.

ACKNOWLEDGMENTS

This material was supported through NASA Grant No. 80NSSC19K0974 from the NASA Innovation Advanced Concepts Program. D.K. acknowledges support from National Science Foundation for its Research Experiences for Undergraduates program through Grant No. EEC-1560424. The authors are grateful for discussions with H. Morgan and C. Limbach and the supercomputing resources from Texas A&M University and Stanford University.

[1] K. C. Neuman and A. Nagy, Nat. Methods **5**, 491 (2008).
[2] J. R. Moffitt, Y. R. Chemla, S. B. Smith, and C. Bustamante, Annu. Rev. Biochem. **77**, 205 (2008).
[3] L. Anderegg, L. W. Cheuk, Y. Bao, S. Burchesky, W. Ketterle, K.-K. Ni, and J. M. Doyle, Science **365**, 1156 (2019).
[4] A. W. Snyder and J. D. Love, *Optical Waveguide Theory* (Springer US, New York, 1984).
[5] A. Melloni, R. Costa, G. Cusmai, and F. Morichetti, Int. J. Mater. Prod. Technol. **34**, 421 (2009).
[6] P. Cheben, P. J. Bock, J. H. Schmid, J. Lapointe, S. Janz, D.-X. Xu, A. Densmore, A. Delâge, B. Lamontagne, and T. J. Hall, Opt. Lett. **35**, 2526 (2010).
[7] E. Agrell, M. Karlsson, A. Chraplyvy, D. J. Richardson, P. M. Krummrich, P. Winzer, K. Roberts, J. K. Fischer, S. J. Savory, B. J. Eggleton, *et al.*, J. Opt. **18**, 063002 (2016).
[8] W. Pötz and P. Kocevar, Phys. Rev. B **28**, 7040 (1983).
[9] P. Barker and M. Charlton, New J. Phys. **14**, 045005 (2012).
[10] P. H. Jones, O. M. MaragÃ², and G. Volpe, *Optical Tweezers: Principles and Applications* (Cambridge University Press, Cambridge, 2015).
[11] A. Ashkin, Phys. Rev. Lett. **24**, 156 (1970).
[12] A. Ashkin, Phys. Rev. Lett. **40**, 729 (1978).
[13] J. E. Bjorkholm, R. R. Freeman, A. Ashkin, and D. B. Pearson, Opt. Lett. **5**, 111 (1980).
[14] D. Pearson, R. Freeman, J. Bjorkholm, and A. Ashkin, Appl. Phys. Lett. **36**, 99 (1980).
[15] S. A. Akhmanov, A. P. Sukhorukov, and R. Khokhlov, Sov. Phys. Usp. **10**, 609 (1968).
[16] M. V. Allmen and A. Blatter, *Laser-Beam Interactions with Materials: Physical Principles and Applications*, Springer Series in Materials Science Vol. 2 (Springer, Berlin, 2013).
[17] G. R. Hadley, Opt. Lett. **16**, 624 (1991).
[18] G. R. Hadley, IEEE J. Quantum Electron. **28**, 363 (1992).
[19] J. Goodman, *Introduction to Fourier Optics*, 3rd ed. (Roberts & Company Publishers, Greenwood Village, 2005).
[20] R. Boyd, *Nonlinear Optics*, 3rd ed. (Academic, New York, 2008).
[21] J. D. Jackson, *Classical Electrodynamics* (American Association of Physics Teachers, College Park, 1999).
[22] A. Yariv, *Introduction to Optical Electronics* (Holt, Rinehart and Winston, New York, 1971).
[23] A. Ashkin, *Optical Trapping and Manipulation of Neutral Particle Using Lasers: A Reprint Volume With Commentaries* (World Scientific, Singapore, 2006).
[24] M. S. Safronova, B. Arora, and C. W. Clark, Phys. Rev. A **73**, 022505 (2006).
[25] C. Foot, *Atomic Physics* (Oxford University Press, Oxford, 2005).
[26] Computational Chemistry Comparison and Benchmark Database, release 21, Experimental polarizabilities, https://cccbdb.nist.gov/pollistx.asp (NIST, Gaithersburg, 2020).
[27] A. Ashkin, Proc. Natl. Acad. Sci. U.S.A. **94**, 4853 (1997).
[28] R. Grimm, M. Weidemüller, and Y. B. Ovchinnikov, Adv. At. Mol. Opt. Phys. **42**, 95 (2000).

[29] J. W. Thomas, *Numerical Partial Differential Equations: Finite Difference Methods*, Texts in Applied Mathematics Vol. 22 (Springer, New York, 2013).

[30] D. Yevick, J. Yu, and Y. Yayon, J. Opt. Soc. Am. A **12**, 107 (1995).

[31] W. P. Huang, C. L. Xu, W. Lui, and K. Yokoyama, IEEE Photon. Technol. Lett. **8**, 649 (1996).

[32] J. Verboncoeur, J. Comput. Phys. **174**, 421 (2001).

[33] T. Charoy, J.-P. Boeuf, A. Bourdon, J. A. Carlsson, P. Chabert, B. Cuenot, D. Eremin, L. Garrigues, K. Hara, I. D. Kaganovich, *et al.*, Plasma Sources Sci. Technol. **28**, 105010 (2019).

[34] K. Hara and S. Tsikata, Phys. Rev. E **102**, 023202 (2020).

[35] P. Kumar, K. Yu, R. Zgadzaj, L. D. Amorim, M. Downer, J. Welch, V. N. Litvinenko, N. Vafaei-Najafabadi, and R. Samulyak, Phys. Plasmas **26**, 083106 (2019).

[36] I. D. Boyd and T. E. Schwartzentruber, *Nonequilibrium Gas Dynamics and Molecular Simulation*, Cambridge Aerospace Series (Cambridge University Press, Cambridge, 2017).

[37] T. Tisovský and T. Vít, EPJ Web Conf. **143**, 02131 (2017).

[38] E. Roohi and S. Stefanov, Phys. Rep. **656**, 1 (2016).

[39] A. Snyder and J. Love, *Optical Waveguide Theory* (Springer US, New York, 2012).

[40] J. Keaveney, I. G. Hughes, A. Sargsyan, D. Sarkisyan, and C. S. Adams, Phys. Rev. Lett. **109**, 233001 (2012).

[41] F. Andreoli, M. J. Gullans, A. A. High, A. Browaeys, and D. E. Chang, Phys. Rev. X **11**, 011026 (2021).